Formation and Healing of Defects in Atomically Thin GaSe and InSe

David G. Hopkinson,[1,2] Viktor Zólyomi,[1,3] Aidan P. Rooney,[2] Nick Clark,[1,2] Daniel J. Terry,[1,3] Matthew Hamer,[1,3] David J. Lewis,[2] Christopher S. Allen,[4,5] Angus I. Kirkland,[4,5] Yuri Andreev,[6] Zakhar Kudrynskyi,[7] Zakhar Kovalyuk,[8] Amalia Patanè,[7] Vladimir I. Fal'ko,[1,3] Roman Gorbachev,[1,3] Sarah J. Haigh[1,2*]*

1. National Graphene Institute, University of Manchester, Booth Street East, M13 9PL, United Kingdom

2. School of Materials, University of Manchester, Oxford Road, Manchester, M13 9PL, United Kingdom

3. School of Physics and Astronomy, University of Manchester, Oxford Road, M13 9PL, United Kingdom

4. Electron Physical Sciences Imaging Centre, Diamond Light Source Ltd., Didcot, Oxfordshire, OX11 0DE, United Kingdom

5. Department of Materials, University of Oxford, Parks Road, Oxford, OX1 3PH, United Kingdom

6. National Tomsk State Research University, 634050 Tomsk, Russian Federation

7. School of Physics and Astronomy, University of Nottingham, Nottingham, NG7 2RD, United Kingdom

8. Institute for Problems of Materials Science, National Academy of Sciences of Ukraine, Chernivtsi Branch, 58001 Chernivtsi, Ukraine

Abstract:

GaSe and InSe are important members of a class of 2D materials, the III-VI metal monochalcogenides, which are attracting considerable attention due to their promising electronic and optoelectronic properties. Here an investigation of point and extended atomic defects formed in mono-, bi-, and few-layer GaSe and InSe crystals is presented. Using state-of-the-art scanning transmission electron microscopy (STEM), it is observed that these materials can form both metal and selenium vacancies under the action of the electron beam. Selenium vacancies are observed to be healable; recovering the perfect lattice structure in the presence of selenium or enabling incorporation of dopant atoms in the presence of impurities. Under prolonged imaging, multiple point defects are observed to coalesce to form extended defect structures, with GaSe generally developing trigonal defects and InSe primarily forming line defects. These insights into atomic behavior could be harnessed to synthesize and tune the properties of 2D post transition metal monochalcogenide materials for optoelectronic applications.

KEYWORDS: InSe, GaSe, 2D materials, point defects, graphene, post-transition metal chalcogenides, III-VI semiconductors

Layered III-VI post transition metal monochalcogenides, such as GaS, GaSe, InS, and InSe, have recently generated much interest within the expanding field of 2D materials beyond graphene.[1] In particular, GaSe and InSe have shown excellent optoelectronic properties, with strong second harmonic generation reported in monolayers of both materials,[2,3] and potential photonic applications.[4,5] These almost lattice-matched films possess high electron mobility (values over 1000 $cm^2V^{-1}s^{-1}$ reported in few layer InSe devices) and thickness-dependent, tunable band-gaps,[6–10] a desirable combination lacking in graphene and most transition metal dichalcogenides (TMDs). In contrast to most TMDs (for example MoS_2),[11–13] both GaSe and InSe possess a direct bandgap in bulk form, which transitions to an quasi-direct bandgap when reduced to the monolayer limit.[14–16] These properties have been successfully applied in few-layer photodetection and field effect devices,[6,9,17–21] and when used together in GaSe/InSe heterostructures, have shown tunable photoemission from interlayer excitons.[10]

The performance of devices based on GaSe and InSe can be affected by the presence of impurities or by exposure to air, light and/or moisture.[7,22,23] As an example, it is generally considered that the presence of selenium vacancies in InSe and their interaction with ambient oxygen species underpins the loss of ambipolarity in InSe FET devices,[23] and is also a cause of the lower ambient stability of InSe relative to expectation.[24] However, in order to fully understand the role of point defects in determining the properties of optoelectronic devices based on III-VI post transition metal monochalcogenides, it is necessary to characterize their structure and dynamic behavior. Previous transmission electron microscopy (TEM) investigations of these few layer monochalcogenides have been limited to structural verification of monolayer GaSe[25] and InSe crystals.[3] Here the formation and stability of atomic vacancy and extended defects in monolayer and few-layer GaSe and InSe is investigated using low voltage, aberration-corrected

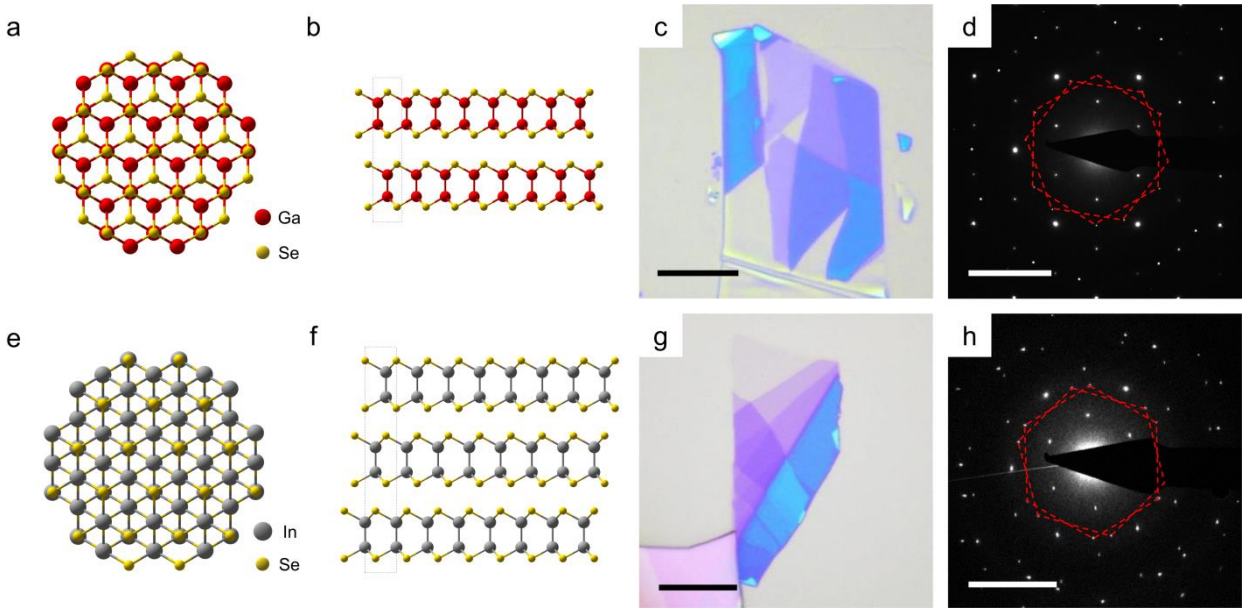

Figure 1 – **Atomic structure and TEM characterisation of few layer GaSe and InSe crystals**. Atomic models of one unit cell thickness of ε-GaSe (a, b) and γ-InSe (e, f), projected along [001] (a, e) and [100] (b, f). (c, g) Optical images of mechanically exfoliated GaSe (c) and InSe (g) crystals prior to graphene encapsulation. Scale bars: 10 μm. (d, h) Selected area electron diffraction patterns for graphene encapsulated few-layer GaSe and InSe, respectively. The 1st order reflections due to the graphene are indicated with red hexagons. Scale bars: 5 nm^{-1}.

scanning transmission electron microscope (STEM) imaging and image simulation, combined with density functional theory (DFT) calculations and electron energy loss spectroscopy (EELS).

The crystal structure of GaSe and InSe consists of van der Waals bonded layers, with each layer comprising four parallel planes of atoms in the order VI-III-III-VI (*e.g.* Se-Ga-Ga-Se, see Figure 1). The individual layers exhibit three-fold honeycomb symmetry and are covalently bonded in-plane. As with most 2D materials, the layer stacking sequence is essential in determining their band structure, with $2H_b$ and 3R stacking (commonly referred to as ε and γ phases) being the most thermodynamically stable polytypes for bulk GaSe and InSe, respectively.[26] These polytypes are illustrated in Figure 1a, 1b, 1e and 1f, and have unit cells

containing n layers, where n = 2 for $2H_b$ and n = 3 for 3R, giving rise to hexagonal (P-6m2) and rhombohedral (R3m) stacking symmetries, respectively.

To enable atomic resolution characterization of these highly beam sensitive materials, few layer GaSe and InSe crystals were encapsulated between two graphene sheets. Graphene encapsulation in an argon glovebox has been previously employed to improve the stability of 2D materials when exposed to high resolution imaging with a focused STEM electron probe.[27–29] The graphene also serves to isolate the material from the air but trace oxygen, carbon, hydrogen and silicon impurities can become trapped beneath the graphene sheets, even when dry peel encapsulation is performed in an inert atmosphere.[30] The trapped contamination provides a source of impurities and therefore enables the study of lattice doping with atomic resolution.

Results/Discussion

InSe and GaSe TEM specimens were prepared by exfoliation of the bulk crystals in an inert argon gas environment to produce flakes that ranged in thickness from 1-5 layers, as determined by the optical contrast (Figure 1c and g). The materials were then encapsulated between two graphene sheets to protect them from atmospheric degradation as well as to reduce electron beam induced radiation damage.[27,28] Selected area electron diffraction (SAED) patterns agree with those expected for few layer GaSe and InSe and also show the reflections associated with the two encapsulating graphene sheets (Figure 1d and h). Monolayer regions are identified using optical contrast prior to encapsulation and by atomic resolution annular dark field (ADF) STEM imaging, with the latter demonstrating an excellent qualitative match to ADF multislice image simulations as shown in Figure 2. The encapsulating graphene layers have been neglected from the ADF STEM defect simulations as their relative lateral position is unknown and they were found to have a negligible effect on the relative intensity of different columns (as shown in

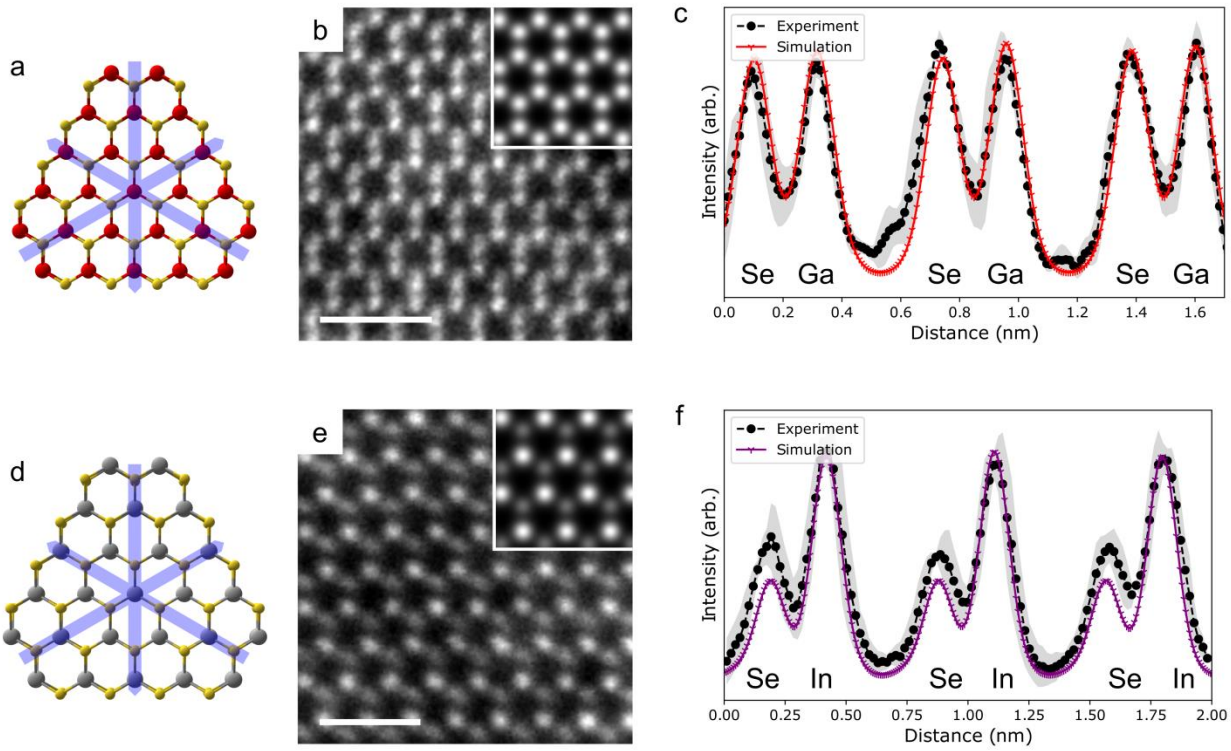

Figure 2 – **ADF STEM imaging of monolayer GaSe and InSe.** (a, d) Atomic models of monolayer GaSe and InSe, respectively, both projected along [001] with blue arrows indicating the directions of the line profiles shown in (c) and (f). (b, e) Time averaged ADF STEM images of monolayer GaSe (averaged over 8 frames) and InSe (averaged over 42 frames), respectively, with corresponding image simulations inset. All scale bars: 1 nm. (c, f) Comparison of normalized experimental and simulated ADF intensity line profiles. Experimental profiles were averaged for the equivalent [110], [1-20], and [-210] armchair directions (indicated by the blue arrows in a and d), with the grey shading indicating one standard deviation error.

Figure S1). In GaSe, the relative positions of the gallium and selenium lattice sites could not be distinguished from the ADF intensity alone. However, as the selenium-selenium spacing projected along the z-axis is larger than the gallium-gallium spacing, a given tilt away from the [001] zone axis causes a greater lateral shift for the selenium atoms than the gallium, revealing

the relative location of the two atomic columns. For example, in Figure 2b there is a larger shift in the atomic columns of the sites at the bottom of each atomic hexagon compared to the top, revealing that in this hexagon the selenium sites form a downward pointing triangle and the gallium an upward pointing triangle.

When irradiated with the electron beam, both materials are observed to form point vacancy defects (Figures 3 and 4 show examples for GaSe and InSe respectively). By performing ADF STEM intensity line profile analysis and comparing the results with images simulated from relaxed structures obtained by DFT, it is possible to qualitatively investigate such atomic defects. In GaSe, vacancies are observed on both gallium and selenium lattice sites with the defect in Figure 3b showing a good match to the expected contrast of a gallium vacancy. Selenium site defects were also observed but comparison with simulations revealed that these defects are likely to be substituted with light atom impurities (Figure 3f). The most likely available light dopant species is considered to be oxygen, but other light impurities, such as nitrogen or carbon, are also possible, as discussed later. Point vacancy defects are also observed in monolayer InSe but here no evidence was found to support light atom substitution. For example, in Figure 4b, the defect at the indium site is a good match to a pristine indium vacancy and the defect at the selenium site in Figure 4f is a better match to a selenium vacancy, rather than a light atom substitution (such as oxygen). The effect on the ADF intensity of a selenium site defect is primarily observed not at the selenium site itself but at the adjacent metal sites. This is due to the missing chalcogenide ion causing a tilting of the neighboring Ga_2/In_2 columns, with the tilt being reduced by the substitution of a stabilizing dopant. Small differences between the experimental and predicted ADF intensities in Figures 2-4 are explained by the presence of a small amount of hydrocarbon contamination on the exterior surface of the graphene encapsulation which introduces a varying

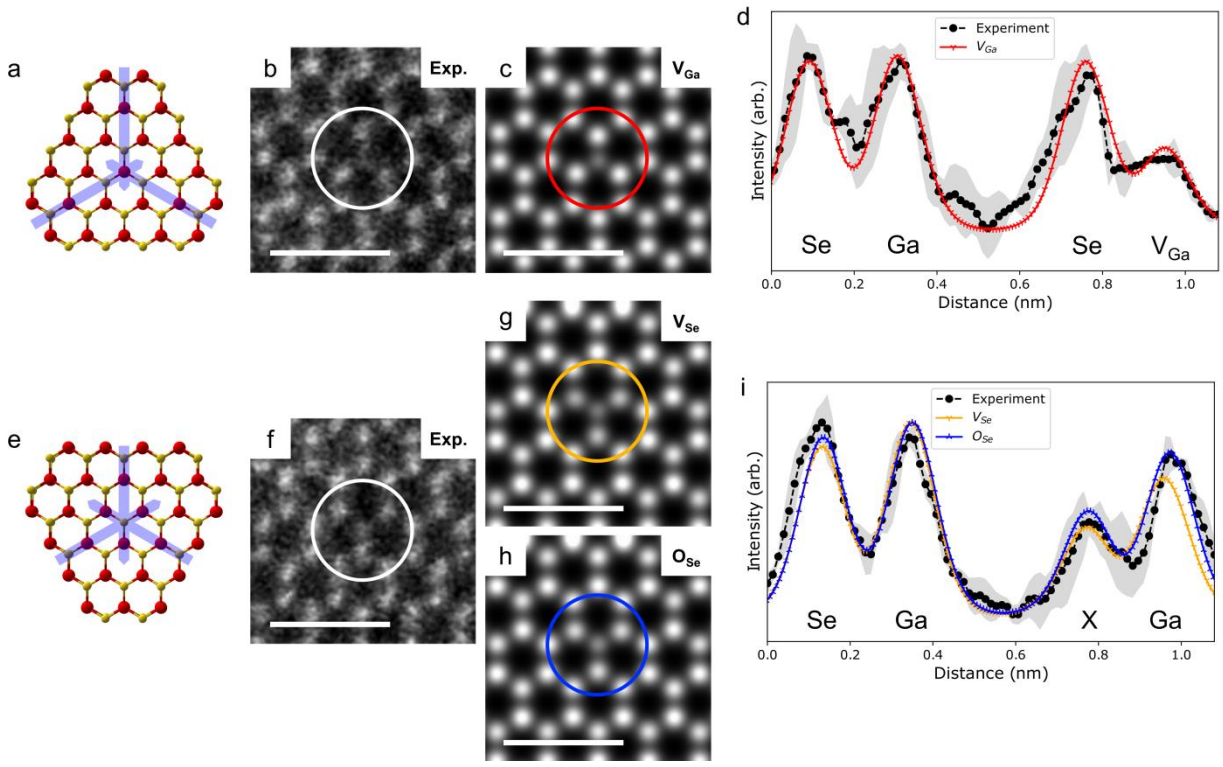

Figure 3 – **Identification of point defects in monolayer GaSe.** (a, e) Atomic models of monolayer GaSe with corresponding line profile directions indicated for gallium and selenium site defects. (b, f) Experimental images of a point defect at a gallium site and at a selenium site, respectively. (c, g, h) Simulated ADF images of a gallium monovacancy, V_{Ga}, a selenium monovacancy, V_{Se}, and an oxygen substitution, O_{Se}. All scale bars: 1 nm. (d, i) Comparison of normalized experimental and simulated ADF intensity across the defects in (c, g, h). Experimental profiles were averaged for the symmetrically equivalent [110], [1-20], and [-210] armchair directions (indicated by the blue lines in a and e), with the grey shading indicating one standard deviation error. The position of the defect site on the line scan is indicated by V_{Ga} or X.

background to the images. In Figure 2, time averaging is used to improve the signal-to-noise ratio and hence increase the confidence of the image analysis. However, this averaging procedure is not possible in Figures 3 and 4 due to the transient nature of the atomic point defects

from frame to frame. This, together with a small sample tilt, prevents a fully quantitative analysis of the dopant species from these images.

In order to better understand the stability and mobility of point defects in this class of 2D materials, beam-induced defect migration in both monolayer GaSe and InSe is investigated (Figure 5). In monolayer regions of both materials with low contamination, vacancies are observed to form, travel to adjacent crystal positions and then recombine with a relevant adatom to completely recover the perfect lattice (healing). In relatively clean areas of the sample, most single point defects heal within approximately 10s of continuous imaging (cumulative electron fluence of ~1.5 x 10^6 $e^-Å^{-2}$). In this time vacancy hopping behavior is observed to occur in to nearest neighbor or next nearest neighbor positions and defect diffusion is generally limited to <2 nm from the initial formation site before healing.

The adatoms liberated from vacancy formation are found to be far more mobile than the vacancies themselves, as they are generally not observed in the vicinity of their vacancy during imaging. This fast surface diffusivity could explain why selenium vacancies are sometimes filled by impurity species rather than the original selenium atom, even in apparently clean regions of the crystal. In contrast, in crystal regions with high levels of trapped contamination, the point defects did not re-heal but rapidly multiplied, resulting in the local destruction of the crystal at an electron fluence of <1 x 10^6 $e^-Å^{-2}$. This difference in behavior for clean *versus* contaminated crystal regions suggests than when impurity species are present in the vicinity of a selenium vacancy, dopant substitution is favored over recovery of the original lattice. This conclusion is supported by the DFT calculations which found that oxygen substitution is energetically more favorable than healing of the original lattice (see Figure 5l).

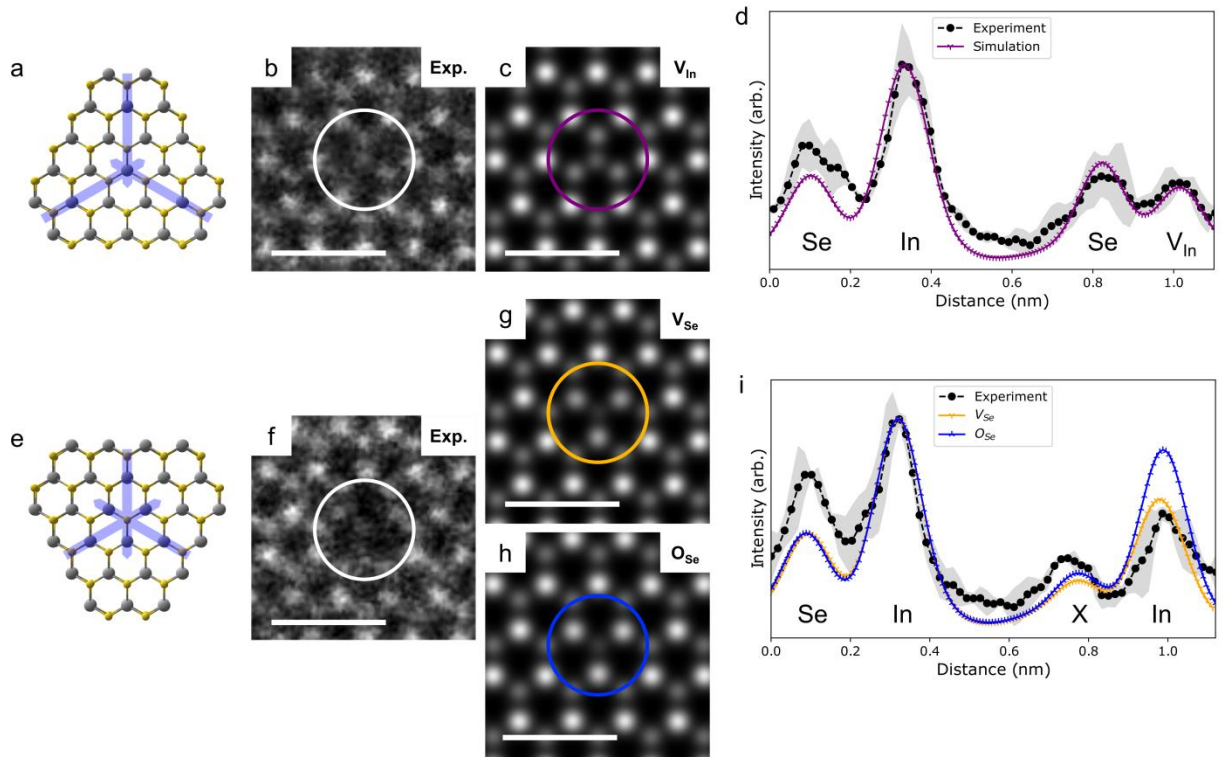

Figure 4 – **Identification of point defects in monolayer InSe.** (a, e) Atomic models of monolayer InSe, with line profile directions indicated for indium and selenium site defects. (b, f) Experimental images of a point defect at an indium site and a selenium site respectively. (c, g, h) Simulated ADF images of an indium monovacancy, V_{In}, a selenium monovacancy, $V_{Se,}$ and an oxygen substitution, O_{Se}. All scale bars: 1 nm. (d, i) Comparison of normalized experimental and simulated ADF intensity across the defects in (c, g, and h). Experimental profiles were averaged for the symmetrically equivalent [110], [1-20], and [-210] armchair directions (indicated by the blue lines in a and e) with the grey shading indicating one standard deviation error. The position of the defect site on the line scan is indicated by V_{In} or X.

In order to understand the mechanism of defect formation, the elastic Mott scattering cross section the maximum energy transfer and the displacement threshold energies for the experiments have been calculated. These calculations demonstrate that the intrinsic knock-on damage threshold for selenium (or gallium/indium) in GaSe or InSe is considerably greater than

the energy available in an 80 keV electron beam, even for atoms adjacent to pre-existing defects (see Supplementary Figure S4). It is therefore unlikely that the irradiation induced defects observed are produced *via* direct knock-on damage (sputtering) of the material. In contrast, light atom molecules and hydrocarbons are well known to be highly susceptible to knock-on damage at 80 kV.[31,32]

Consequently, the unavoidable presence of an oxygen-containing hydrocarbon residue trapped between the encapsulating graphene sheets and the III-VI crystal is likely to serve as a source of oxidative radical species generated through interaction with the electron beam. It is therefore suggested that selenium vacancies can be formed by interaction with oxidative species produced through radiolytic, interatomic Auger decay processes.[33,34] Chalcogenide vacancies have been predicted as energetically favorable sites for O_2 and H_2O adsorption and dissociation in both GaSe and InSe,[23,35,36] and so it follows that beam-induced vacancy formation in the presence of oxygen-rich hydrocarbon contamination would result in the oxidation of the nearby gallium or indium. With the reduced bonding energy typically associated with atoms neighboring defect sites and the energetic favorability of oxygen substitution (see Figure 5l), this provides a possible explanation for the accelerated degradation observed in the presence of both chalcogenide vacancy defects and residual contamination.

The evolution of extended defects in clean (or relatively low contamination) crystal regions differs between GaSe and InSe. In few layer GaSe, point defect clusters typically form stable trigonal defects during prolonged imaging (Figure 6a-d) with facets aligned along zigzag crystallographic directions ([010], [-100], and [1-10]). These trigonal defects form where complete layers are removed without significant damage to the adjacent layer(s), with the liberated atoms believed to migrate between the graphene sheets to form amorphous or semi-

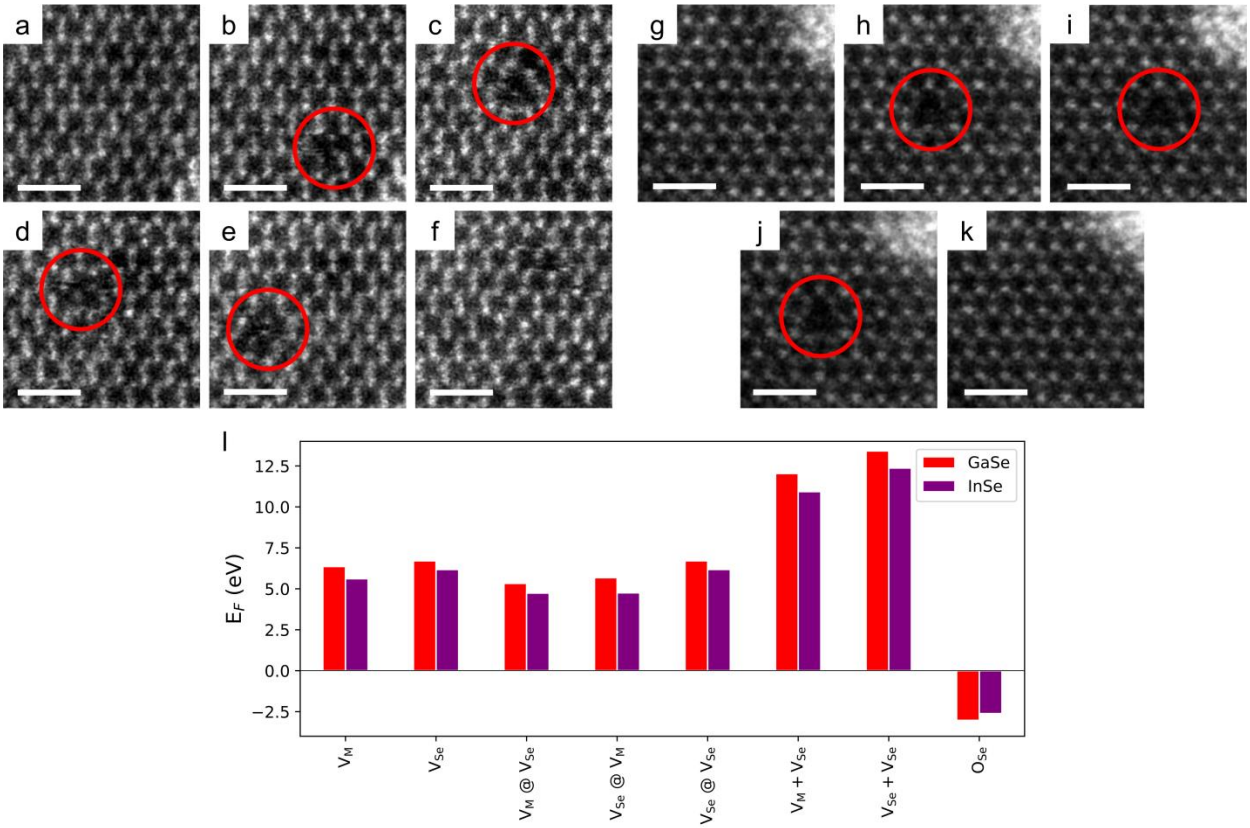

Figure 5 – **Point defect migration, healing, and energetics in monolayer GaSe and InSe.** (a-f) Drift corrected ADF time series of formation, motion, and healing of a small defect cluster in monolayer GaSe. (g-k) Drift corrected ADF time series of formation, motion, and healing of a selenium monovacancy in monolayer InSe. All scale bars: 1 nm. Time between frames is ~1s with an electron fluence per frame of ~1.3 x 10^5 $e^-Å^{-2}$. Both image series are provided as videos in the supporting information (Supplementary Video S1 and S2, respectively). (l) Point defect formation energies, E_F, in GaSe and InSe. V_M corresponds to the relevant metal vacancy, '@' indicates a vacancy forming adjacent to a pre-existing vacancy, and '+' indicates a vacancy pair. Tabulated defect energies are provided in the supplementary information (Supplementary Table S1).

crystalline clusters that are observed at nearby edges and other features. These trigonal defects are observed in both ε-stacked GaSe (Figure 6c, d) and AA-stacked GaSe (Figure 6b) (which

appears due to stacking faults that develop in the crystal; differences in crystal stacking are considered in detail later).

For example, this defect behavior exposes local regions of pristine monolayer crystal in bilayer material (Figure 6b) and similar trigonal defect structures are observed in several different crystals and in regions with different local stacking and thicknesses. Although the some of these defects form as a result of prolonged electron beam irradiation (fluence $>10^6$ $e^-Å^{-2}$), the trigonal defects in bilayer GaSe (Figure 6c, d) are present in the first images captured, suggesting the morphology observed is also a stable form of intrinsic defect structure in GaSe. Supporting this, similar trigonal defects have also been observed *via* STM in GaSe crystals by Ohta *et al*[37] and optically by Li *et al*[25] in GaSe monolayers.

In contrast, extended defects in few layer InSe adopt a different morphology, showing linear structures (Figure 6e-h) that are similar to those seen in some TMD crystals, including MoS_2 and $MoSe_2$.[38–41] These linear defects are aligned along the zigzag directions ([010], [-100], and [1-10]), the same geometry as is observed for single and double width vacancy lines reported for MoS_2,[38] and parallel to the edges of the trigonal defects observed in GaSe. At high vacancy concentrations these linear defects coalesce to form trigonal gaps or islands (Figure 6g). It is possible that the presence of intrinsic trigonal defects in GaSe may contribute to its lower ambient stability relative to InSe, due to the introduction of exposed edges that are susceptible to chemical attack.

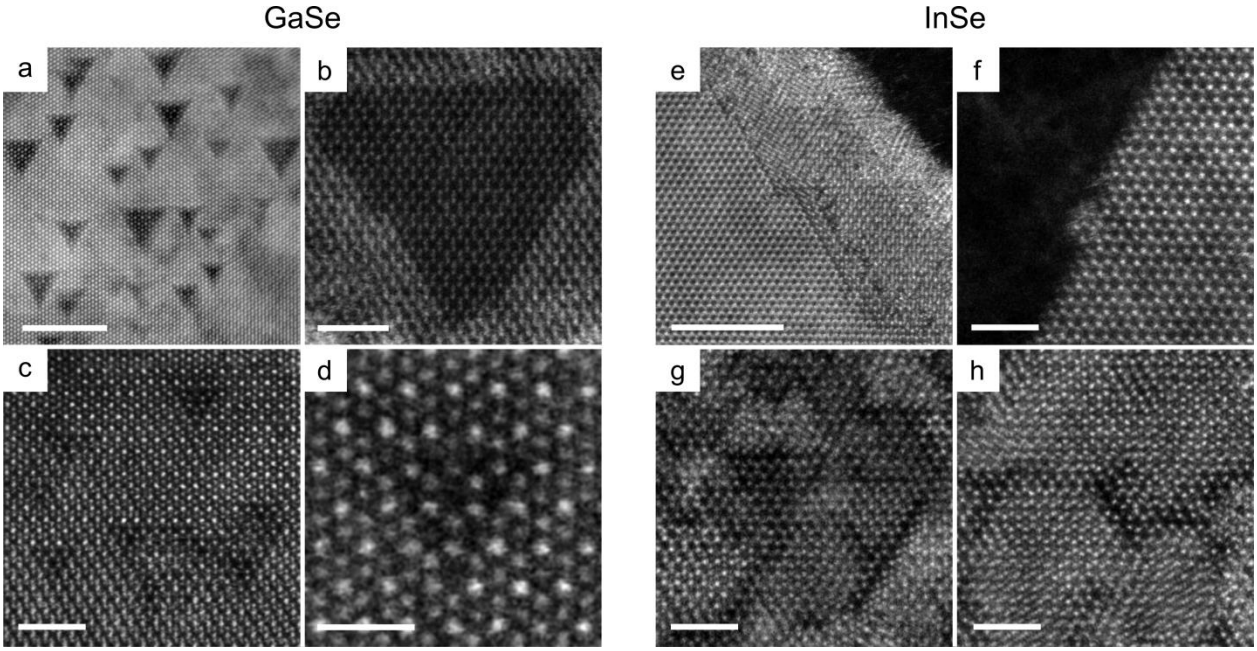

Figure 6 – **Comparison of extended defects in GaSe and InSe.** (a) Time averaged ADF image of clustered, stable trigonal defects in thick (>10 layer) GaSe after a cumulative fluence of ~8 x 10^6 $e^-Å^{-2}$. Scale bar: 5 nm. (b) Trigonal defect in bilayer AA-stacked GaSe exposing a monolayer region of crystal. Scale bar: 2 nm. (c) Clustered trigonal defects in bilayer ε-GaSe. This was the first image captured of this area of crystal, with a cumulative fluence of ~1.3 x 10^5 $e^-Å^{-2}$. Scale bar: 2 nm. (d) Detail of trigonal defect shown top right in (c). Scale bar: 1 nm. (e) Atomically sharp step edge neighboring a semi-crystalline crack edge in few-layer InSe. Scale bar: 5 nm. (f) Atomically sharp, reconstructed edge in monolayer InSe. Scale bar: 2 nm. (g, h) Selenium vacancy zigzag line defects in bilayer γ-InSe. Scale bar: 2 nm.

The difference in the observed morphologies of the extended defects can be assigned to the different behavior of the post transition metals (gallium and indium). Trigonal lattice defects like those seen in GaSe tend to form when the energy needed to remove atoms is similar for both species (as for electron beam induced knock-on damage of hBN).[42–44] Linear defects form in TMDs where the probability of removing the chalcogenide is much greater than the transition

metal. This is evident in Figure 6b, where a mixture of gallium-terminated (reconstructed Klein-like[45,46]) and selenium-terminated (zigzag) edges are present along the upper step edge of the facet in bilayer GaSe, whereas the features in Figures 6g and h of bilayer InSe show a predominance of indium termination. Based on these differences in extended defect structure, it can be ascertained that in GaSe, both gallium and selenium vacancies can be formed under electron irradiation. However, in InSe, the predominance of selenium vacancy-based defects suggests preferential formation of selenium vacancies over indium vacancies.

Whilst investigating these materials, other larger scale defects including cracks and local stacking faults were observed. Both structures are likely to be the result of mechanical stress applied to the crystal during exfoliation and encapsulation, combined with oxidative damage due to compromised encapsulation or trapped contamination. For example, cracks provide a fast route for ingress of oxidative species as the graphene often cannot form a complete hermetic seal due to abrupt local topographic changes. This results in an oxidized layer either side of the crack with a width of 5-10 nm (Figure 6e and 7b). Amorphous material and local vacancies are observed neighboring the crack, but beyond these the crystal maintains a perfect lattice structure suggesting that the oxidized layer forms a passivation barrier preventing further degradation (as observed for black phosphorus).[47,48]

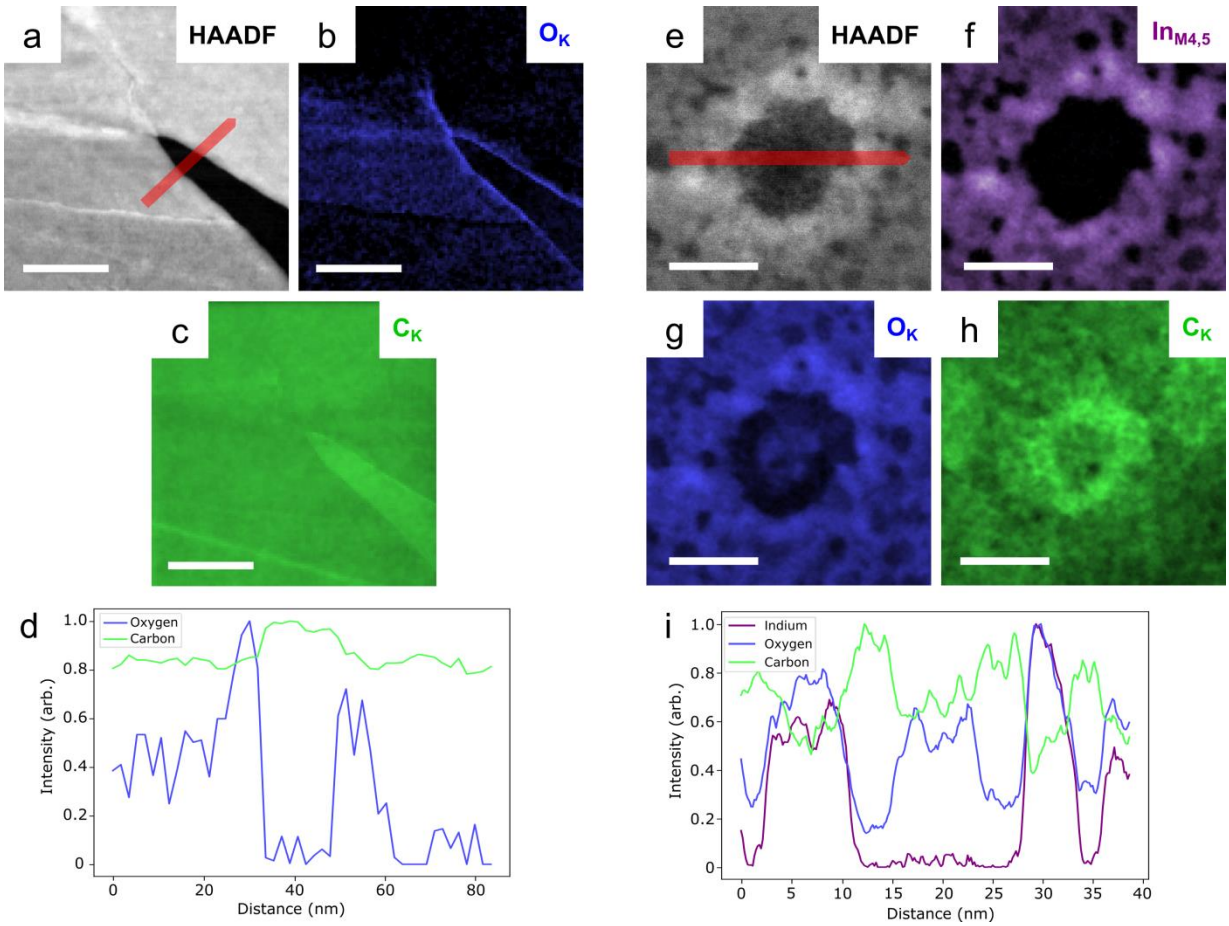

Figure 7 – **EELS elemental mapping and intensity profiles for damaged regions in GaSe and InSe.** (a-c) ADF STEM image, oxygen, and carbon EELS maps at a cracked region in GaSe. Scale bars: 50 nm. (d) EELS intensity profiles across the crack region indicated with a red arrow in (a). (e-h) ADF STEM image, indium, oxygen, and carbon EELS maps of a hydrocarbon-filled bubble in degraded InSe. Scale bars: 10 nm. (i) EELS intensity profiles across the hydrocarbon region indicated in (e).

Figure 7b shows the ingress of oxygen along creases alongside and radiating from a crack tip as measured by EELS mapping. Elemental mapping of a trapped hydrocarbon-rich bubble after imaging (Figure 7e-h) shows that whilst indium and oxygen are strongly co-localized outside the bubble, no indium is observed within the center. This suggests that the contamination has etched

the crystal, forming a thicker amorphous oxide layer at the edge. In addition, the hydrocarbon bubble has an outer rim (~5 nm thick) that is depleted in oxygen relative to the center (Figure 7g), supporting the hypothesis that hydrocarbon contamination is the source of oxygen.

Finally, the presence of multiple stacking faults in both GaSe and InSe few layer crystals is identified. The ability of van der Waals crystals to exist in multiple different low energy stacking configurations, each with different optical and electronic properties, can provide a potential route for tuning the material's behavior for different applications.[49–52] Both GaSe and InSe crystals are known to occur in several different polytypes that are structurally equivalent except for their stacking sequence.[26,53] However, the optoelectronic properties, such as the bandgap, are predicted to vary for different polytypes.[14] It is therefore important to understand the presence and nature of stacking defects in order to accurately interpret optoelectronic device behavior.

Figure 8 shows stacking faults in bilayer GaSe and InSe, demonstrating the transition from ε-/γ- to AA-stacking. Whilst AA-stacking (in effect 1H symmetry) is not expected to occur naturally in either material, ADF intensity analysis confirms the presence of this stacking over large areas of the crystal (Supplementary Figure S10). It can be seen in Figure 8 that both stacking faults comprise of a shear translation of (1/3) [-210]. The fault boundaries are oriented ~60° to the direction of the shear (see Supplementary Figure S9), similar to the 60° shear partial dislocations previously observed in graphene bilayers, which generate AB ↔ AC transitions.[54] The boundary between the two pristine stacking regions extends over a distance of greater than 10 nm, similar to faults reported in other 2D chalcogenides.[55,56] Previous work by Zhou *et al* has identified a γ ↔ β stacking transition in bilayer InSe,[3] but their characterization found the boundary to be atomically abrupt (discussed in the Supporting Information). The difference between this and the data presented in this work is easily attributed to the different synthesis and

processing for their material: Zhou *et al* studied InSe synthesized by a bottom-up PVD method, whilst this work utilizes top-down mechanically exfoliated materials. It is suggested that in bilayers, abrupt stacking boundaries result from different stacking regions impinging during crystal growth, whereas the extended boundaries observed here are not intrinsic to the bulk crystal but form as a result of mechanical stress during mechanical exfoliation and encapsulation.[57]

The extended stacking faults are of interest as they introduce sizable regions of different crystal symmetry. This is particularly relevant to InSe, where honeycomb-like hexagonal polytypes generally do not form spontaneously, as opposed to GaSe which exists in four stable stacking phases (β, γ, δ, and ε), of which the β polytype (also called $2H_c$, with $P6_3/mmc$ symmetry) possesses honeycomb symmetry.[26,58] The authors are not aware of any previous experimental or theoretical works that report AA-stacked (1H) InSe or GaSe materials, hence the known effects of hexagonally symmetric β-stacking as well as the possible effects of AA-stacking are considered briefly here. In both GaSe and InSe, when ε- or γ-stacking transitions into β-stacking, it will have an effect on the rules governing spectroscopic selection; since β-stacking is the only stacking order to exhibit inversion symmetry. In vibrational spectroscopy, IR and Raman activity are mutually exclusive in the presence of inversion symmetry, thus a different response is expected in β- compared to ε-/γ- stacked bilayers. In the bulk limit, ε-GaSe is known to exhibit two Raman active modes around 210-215 cm^{-1},[59] while only one of those is Raman active in β-GaSe.[58] The splitting between the two modes is small which would make it challenging to identify ε- or β-stacking from the Raman spectrum alone, demonstrating the importance of gaining a full microstructural understanding of the material when interpreting optical data.

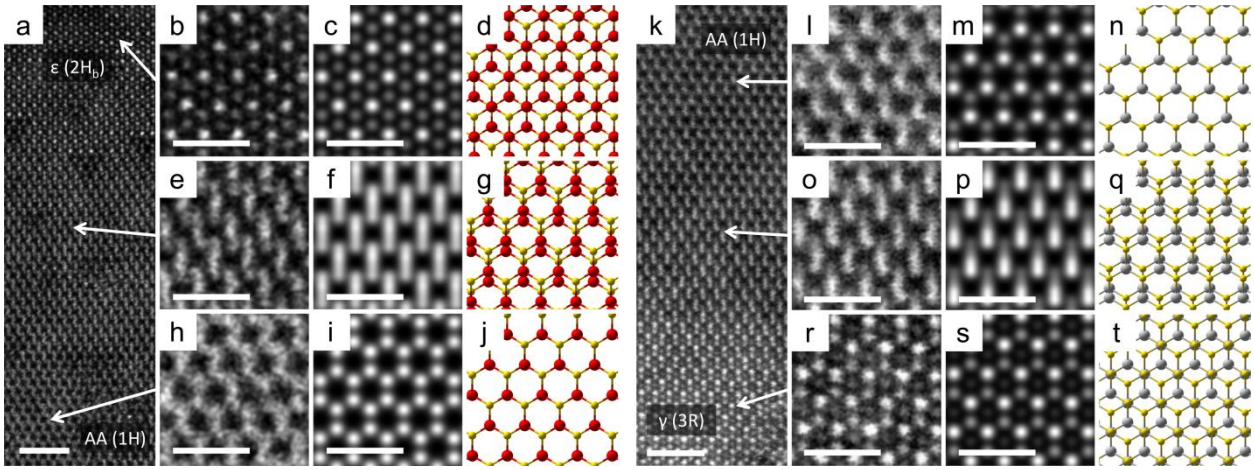

Figure 8 – **Stacking faults in bilayer GaSe and InSe.** (a) ADF image of a stacking transition from ε- to AA-stacking in GaSe. Scale bar: 2 nm. (b, e, h) ADF images, (c, f, i) image simulations, and (d, g, j) structural models showing detail of the ε, intermediate, and AA regions, respectively. Scale bars 1 nm. (h) ADF image of a stacking transition from AA- to γ-stacking in InSe. Scale bar: 2 nm. (l, o, r) ADF images, (m, p, s) image simulations, and (n, q, t) structural models showing detail of the AA, intermediate, and γ regions, respectively. Scale bars: 1 nm.

Similarly, the photoluminescence (PL) excitation energies of InSe and GaSe films are also modulated by stacking order, which matters for both β- and AA-stacking, although this effect is small due to spin-orbit coupling. In the absence of spin-orbit coupling, symmetry forbids the lowest energy optical transition, and while this restriction is lifted by band mixing promoted by spin-orbit interaction,[60] it remains weak, hence the absence of the lowest energy PL line in monolayer InSe.[7] In contrast, whilst ε- or γ-stacking activates this transition, in AA-stacking the retained z/-z reflection symmetry of the crystal forbids the transition which is only enabled by spin-orbit interaction, while in β-stacking the same occurs due to the presence of inversion symmetry. Stacking faults could, in principle, be observed by mapping the PL intensity, as a drop in intensity is likely to occur at AA- and β-stacked regions. However, the relatively poor

spatial resolution of the PL technique, together with the small magnitude of the change in intensity, would make this experimentally challenging. Nevertheless, the results suggest that mechanically exfoliated GaSe and InSe few layer crystals contain cracks and stacking faults which could modify the observed optoelectronic performance. If controlled, the observed stacking changes could provide a route for very fine tuning of the optical properties of devices based on these materials. Mechanically induced stacking faults may also contribute to strain induced emission phenomena observed in both GaSe[5] and InSe.[61]

Conclusions

In summary, experimental data for the structure of point and extended defects in monolayer and few-layer GaSe and InSe, and their evolution under electron beam irradiation have been provided. Both materials were found to form vacancy defects in metal and chalcogenide lattice sites, with the latter sometimes being substituted with a light dopant atom species, likely to be oxygen. During extended imaging, defects are able to migrate and heal in areas of low contamination, potentially providing a route to controlled lattice doping and repair of these materials. Extended vacancy defects were observed to have different morphologies in the two materials; GaSe forming extended trigonal defects similar to those observed in hBN, whilst in InSe formed line defects common to 2D metal chalcogenides. These differing morphologies may explain, in part, the different ambient stabilities of GaSe and InSe. Stacking faults and AA-stacking were also observed in multilayer regions, deviating from the most stable ε- and γ-stacking sequences (GaSe and InSe, respectively), and are associated with stress relaxation. Given the potential for the use of local lattice doping, strain engineering, and stacking changes to tune the optoelectronic properties of III-VI metal monochalcogenides, this structural information provides vital insight towards the experimental realization of emergent properties. The observed

behavior is especially relevant when considering necessary fabrication techniques such as electron beam lithography, due to potential modification of device properties by electron irradiation-induced defects and electron beam-contamination interactions. For example the results suggest that lithographic patterning of encapsulated crystals in the presence of excess selenium may provide a route to reducing oxidative damage.

Methods/Experimental

γ-InSe and ε-GaSe single crystals were grown by a modified Bridgman method[62,63] from high purity(>99.999%) gallium, indium, and selenium source materials. From these bulk crystals, few-layer specimens were mechanically exfoliated by peeling with Nitto Denko BT-150E-CM tape before being pressed onto a Si/SiO_2-90nm wafer (heated to 60°C) which had a thin (~200nm) spin-coated film of poly(propylenecarbonate) on the surface (to improve adhesion).

Suitable flakes were then identified using optical microscopy and picked up with monolayer graphene using the poly(methyl-methacrylate) (PMMA) dry peel transfer technique using a bespoke micromanipulation setup. Following this, a second flake of graphene was picked up from Si/SiO_2-90nm fully encapsulating the specimen while on the PMMA membrane. Exfoliation and transfers took place within an argon glovebox to prevent sample degradation.[64,65]

After full encapsulation with graphene on each side, the specimen was removed from the glovebox and transferred onto a custom SiN TEM grid, using the PMMA dry transfer technique, cutting around the PMMA membrane. To promote adhesion between the specimen and the grid, annealing was performed at 130°C for 5 minutes. To remove polymer on the surface of the specimen, the sample was cleaned by full immersion in acetone, IPA and hexane for 5 minutes each. The specimen was then removed and flash dried with nitrogen to remove any surface solvent residue.

Aberration corrected, annular dark field (ADF) scanning transmission electron microscope (STEM) imaging of GaSe was performed using a JEOL ARM300CF double aberration corrected microscope with a cold FEG electron source, operating at an accelerating voltage of 80 kV, with a beam convergence semi-angle of 32 mrad, probe current of 67 pA and a ADF collection angle of 68-206 mrad. ADF STEM of InSe was performed at 60 kV and 80 kV; at 60 kV, the convergence semi-angle was 31 mrad, with 73 pA probe current and 56-207 mrad collection angle, and at 80 kV, the convergence semi-angle was 32 mrad, with 67 pA probe current and 68-206 mrad collection semi-angle.. All aberrations were individually corrected to better than a pi/4 phase shift at 30 mrad. Selected area electron diffraction (SAED) TEM and STEM elemental analysis using electron energy loss spectroscopy (EELS) was performed using a probe corrected FEI Titan G2 with an X-FEG source operating at 200kV (SAED) and 80kV (EELS). Energy loss spectra were obtained between 150-662 eV and 1050-1562 eV (before zero loss peak alignment), with a dispersion of 0.25 eV. The core loss edges used for model fitting were $In_{M,4,5}$ (443 eV), C_K (284 eV), and O_K (532 eV) edges.

Multislice ADF STEM image simulation was performed using QSTEM,[66] using the above experimental parameters, source size of 1.1 Å, at Scherzer defocus and averaged for 25 randomized phonon configurations. Reference bulk crystal structures were obtained from the Inorganic Crystal Structure Database[67] and processed using the Atomic Simulation Environment.[68] Structural models were rendered using VESTA.[69] EELS analysis was performed using HyperSpy v1.3,[70] with principle component analysis dimensionality reduction to reduce the noise level followed by model fitting of the elemental edges.[71] To aid visualization, all ADF STEM images were Gaussian filtered.

Density functional theory (DFT) as implemented in the VASP code[72] was used to calculate the formation energies of point defects in 5x5 supercells of monolayer InSe and GaSe, and the inter-layer binding energies of pristine bilayer InSe and GaSe. All calculations used a plane-wave basis with a cutoff energy of 600 eV and neglected spin-orbit coupling. A 20 Å separation in the vertical direction was included to model the freestanding 2D crystals in a 3D cell, and in the point defect calculations a 6x6x1 Monkhorst-Pack k-point grid was used. The presence of graphene was neglected in the calculations as no significant charge transfer is expected from graphene to InSe or GaSe, based on recent ARPES measurements of monolayer GaSe with graphene contacts where the Dirac point of graphene is found to be located over 2 eV above the valence band edge of GaSe and over 1 eV below the conduction band edge.[73] For InSe, while charge transfer is possible for n-doped layers, it is small as the layers are atomically thin; therefore, the integral value of the available charge is small.

In the point defect calculations, a full structural relaxation was performed on both InSe and GaSe monolayers in a 5x5 supercell, containing one of the following point defects: a single selenium vacancy, single metal vacancy, metal-selenium divacancy, selenium-selenium divacancy, and selenium to oxygen substitution. The total energies were compared to that of the relaxed pristine 5x5 supercell and defect formation energies were computed as the difference between the total energy of the system after and before the introduction of the defect.

ASSOCIATED CONTENT

Supporting Information.

The Supporting Information is available online.

Tabulated relaxed and unrelaxed DFT defect formation energies for point defects in GaSe and InSe monolayers. Details of displacement cross section and maximum beam energy transfer

calculations. Atomic structures for point defects in monolayer GaSe and monolayer InSe. Details of EELS characterization. (PDF)

Video S1 of defect motion in monolayer GaSe. Scale bar: 1 nm. (AVI)

Video S2 of defect motion monolayer InSe. Scale bar: 1 nm. (AVI)

Video S3 of stable defects in thick GaSe. Scale bar: 5 nm. (AVI)

AUTHOR INFORMATION

Corresponding Authors

* Email: roman@manchester.ac.uk, sarah.haigh@manchester.ac.uk

Author Contributions

D.G.H., V.Z., and S.J.H. wrote the manuscript. D.G.H., A.P.R., S.J.H, and C.S.A. carried out the STEM study. D.G.H. analyzed the imaging data. D.G.H. and S.J.H. performed EELS measurements and N.C. analyzed the EELS data. D.J.T., M.H., and R.G. prepared the TEM samples. V.Z. and V.I.F. performed the first principles calculations and provided theory support. Y.A., Z.Ku., Z.Ko., and A.P. provided the bulk materials. R.G. and S.J.H. supervised the project. All authors commented on the manuscript.

ACKNOWLEDGMENT

The authors would like to thank the Engineering and Physical Sciences Research Council (EPSRC) U.K Grants EP/K016946/1, EP/M010619/1, EP/R031711/1 and EP/P009050/1, the EPSRC Graphene NoWNano CDT, and the Defense Threat Reduction Agency Grant HDTRA1-12-1-0013 for funding. S.J.H. acknowledges funding European Research Council (ERC) under

the European Union's Horizon 2020 research and innovation program (Grant Agreement ERC-2016-STG-EvoluTEM-715502, the Hetero2D Synergy grant, and the European Graphene Flagship Project). V. Z. and V. I. F. acknowledge support from the Graphene Flagship Project, the N8 Polaris service, the ARCHER National UK Supercomputer (RAP Project e547), the Computational Shared Facility at the University of Manchester, and the Tianhe-2 Supercomputing Facility in Guangzhou, China. Z.D.K. acknowledges support from the National Academy of Sciences of Ukraine. A.P. acknowledges support from the Leverhulme Trust. We thank S. J. Magorrian for useful discussions. R.G. acknowledges the Royal Society Fellowship scheme. We thank Diamond Light Source for access and support in use of the electron Physical Science Imaging Centre (Instrument E02 EM16892 and EM17837) that contributed to the results presented here. All original data is available from the corresponding author on request.

REFERENCES

(1) Boukhvalov, D.; Gürbulak, B.; Duman, S.; Wang, L.; Politano, A.; Caputi, L.; Chiarello, G.; Cupolillo, A. The Advent of Indium Selenide: Synthesis, Electronic Properties, Ambient Stability and Applications. *Nanomaterials* **2017**, *7*, 372.

(2) Zhou, X.; Cheng, J.; Zhou, Y.; Cao, T.; Hong, H.; Liao, Z.; Wu, S.; Peng, H.; Liu, K.; Yu, D. Strong Second-Harmonic Generation in Atomic Layered GaSe. *J. Am. Chem. Soc.* **2015**, *137*, 7994–7997.

(3) Zhou, J.; Shi, J.; Zeng, Q.; Chen, Y.; Niu, L.; Liu, F.; Yu, T.; Suenaga, K.; Liu, X.; Lin, J.; Liu, Z. InSe Monolayer: Synthesis, Structure and Ultra-High Second-Harmonic Generation. *2D Mater.* **2018**, *5*, 025019.

(4) Karvonen, L.; Säynätjoki, A.; Mehravar, S.; Rodriguez, R. D.; Hartmann, S.; Zahn, D. R. T.; Honkanen, S.; Norwood, R. A.; Peyghambarian, N.; Kieu, K.; Lipsanen, H.; Riikonen,

J. Investigation of Second- and Third-Harmonic Generation in Few-Layer Gallium Selenide by Multiphoton Microscopy. *Sci. Rep.* **2015**, *5*, 10334.

(5) Tonndorf, P.; Schwarz, S.; Kern, J.; Niehues, I.; Del Pozo-Zamudio, O.; Dmitriev, A. I.; Bakhtinov, A. P.; Borisenko, D. N.; Kolesnikov, N. N.; Tartakovskii, A. I.; Michaelis de Vasconcellos, S.; Bratschitsch, R. Single-Photon Emitters in GaSe. *2D Mater.* **2017**, *4*, 021010.

(6) Balakrishnan, N.; Kudrynskyi, Z. R.; Smith, E. F.; Fay, M. W.; Makarovsky, O.; Kovalyuk, Z. D.; Eaves, L.; Beton, P. H.; Patanè, A. Engineering p – n Junctions and Bandgap Tuning of InSe Nanolayers by Controlled Oxidation. *2D Mater.* **2017**, *4*, 025043.

(7) Bandurin, D. A.; Tyurnina, A. V.; Yu, G. L.; Mishchenko, A.; Zólyomi, V.; Morozov, S. V.; Kumar, R. K.; Gorbachev, R. V.; Kudrynskyi, Z. R.; Pezzini, S.; Kovalyuk, Z. D.; Zeitler, U.; Novoselov, K. S.; Patanè, A.; Eaves, L.; Grigorieva, I. V.; Fal'ko, V. I.; Geim, A. K.; Cao, Y. High Electron Mobility, Quantum Hall Effect and Anomalous Optical Response in Atomically Thin InSe. *Nat. Nanotechnol.* **2017**, *12*, 223–227.

(8) Li, Y.; Wang, T.; Wu, M.; Cao, T.; Chen, Y.; Sankar, R.; Ulaganathan, R. K.; Chou, F.-C.; Wetzel, C.; Xu, C.; Louie, S. G.; Shi, S. Ultrasensitive Tunability of the Direct Bandgap of 2D InSe Flakes *via* Strain Engineering. *2D Mater.* **2018**, *5*, 021002.

(9) Hamer, M. J.; Tóvári, E.; Zhu, M.; Thompson, M. D.; Mayorov, A. S.; Prance, J.; Lee, Y.; Haley, R. P.; Kudrynskyi, Z. R.; Patanè, A.; Terry, D.; Kovalyuk, Z. D.; Ensslin, K.; Kretinin, A. V.; Geim, A. K.; Gorbachev, R. V. Gate-Defined Quantum Confinement in InSe-Based van Der Waals Heterostructures. *Nano Lett.* **2018**, *18*, 3950–3955.

(10) Terry, D. J.; Zólyomi, V.; Hamer, M.; Tyurnina, A. V.; Hopkinson, D. G.; Rakowski, A.

M.; Magorrian, S. J.; Clark, N.; Andreev, Y. M.; Kazakova, O.; Novoselov, K.; Haigh, S. J.; Fal'ko, V. I.; Gorbachev, R. V. Infrared-to-Violet Tunable Optical Activity in Atomic Films of GaSe, InSe, and Their Heterostructures. *2D Mater.* **2018**, *5*, 041009.

(11) Wang, Q. H.; Kalantar-Zadeh, K.; Kis, A.; Coleman, J. N.; Strano, M. S. Electronics and Optoelectronics of Two-Dimensional Transition Metal Dichalcogenides. *Nat. Nanotechnol.* **2012**, *7*, 699–712.

(12) Splendiani, A.; Sun, L.; Zhang, Y.; Li, T.; Kim, J.; Chim, C. Y.; Galli, G.; Wang, F. Emerging Photoluminescence in Monolayer MoS2. *Nano Lett.* **2010**, *10*, 1271–1275.

(13) Mak, K. F.; Lee, C.; Hone, J. C.; Shan, J.; Heinz, T. F. Atomically Thin MoS2: A New Direct-Gap Semiconductor. *Phys. Rev. Lett.* **2010**, *105*, 2–5.

(14) Gomes da Costa, P.; Dandrea, R. G.; Wallis, R. F.; Balkanski, M. First-Principles Study of the Electronic Structure of γ-InSe and β-InSe. *Phys. Rev. B: Condens. Matter Mater. Phys.* **1993**, *48*, 14135–14141.

(15) Mudd, G. W.; Svatek, S. A.; Ren, T.; Patanè, A.; Makarovsky, O.; Eaves, L.; Beton, P. H.; Kovalyuk, Z. D.; Lashkarev, G. V.; Kudrynskyi, Z. R.; Dmitriev, A. I. Tuning the Bandgap of Exfoliated InSe Nanosheets by Quantum Confinement. *Adv. Mater.* **2013**, *25*, 5714–5718.

(16) Lei, S.; Ge, L.; Najmaei, S.; George, A.; Kappera, R.; Lou, J.; Chhowalla, M.; Yamaguchi, H.; Gupta, G.; Vajtai, R.; Mohite, A. D.; Ajayan, P. M. Evolution of the Electronic Band Structure and Efficient Photo-Detection in Atomic Layers of InSe. *ACS Nano* **2014**, *8*, 1263–1272.

(17) Tamalampudi, S. R.; Lu, Y. Y.; Kumar U., R.; Sankar, R.; Liao, C. Da; Moorthy B., K.; Cheng, C. H.; Chou, F. C.; Chen, Y. T. High Performance and Bendable Few-Layered

InSe Photodetectors with Broad Spectral Response. *Nano Lett.* **2014**, *14*, 2800–2806.

(18) Feng, W.; Zheng, W.; Cao, W.; Hu, P. Back Gated Multilayer InSe Transistors with Enhanced Carrier Mobilities *via* the Suppression of Carrier Scattering from a Dielectric Interface. *Adv. Mater.* **2014**, *26*, 6587–6593.

(19) Lei, S.; Wen, F.; Ge, L.; Najmaei, S.; George, A.; Gong, Y.; Gao, W.; Jin, Z.; Li, B.; Lou, J.; Kono, J.; Vajtai, R.; Ajayan, P. M.; Halas, N. J. An Atomically Layered InSe Avalanche Photodetector. *Nano Lett.* **2015**, *15*, 3048–3055.

(20) Chen, Z.; Biscaras, J.; Shukla, A. A High Performance Graphene/Few-Layer InSe Photo-Detector. *Nanoscale* **2015**, *7*, 5981–5986.

(21) Mudd, G. W.; Svatek, S. A.; Hague, L.; Makarovsky, O.; Kudrynskyi, Z. R.; Mellor, C. J.; Beton, P. H.; Eaves, L.; Novoselov, K. S.; Kovalyuk, Z. D.; Vdovin, E. E.; Marsden, A. J.; Wilson, N. R.; Patanè, A. High Broad-Band Photoresponsivity of Mechanically Formed InSe-Graphene van Der Waals Heterostructures. *Adv. Mater.* **2015**, *27*, 3760–3766.

(22) Tan, J. Y.; Avsar, A.; Balakrishnan, J.; Koon, G. K. W.; Taychatanapat, T.; O'Farrell, E. C. T.; Watanabe, K.; Taniguchi, T.; Eda, G.; Castro Neto, A. H.; Özyilmaz, B. Electronic Transport in Graphene-Based Heterostructures. *Appl. Phys. Lett.* **2014**, *104*, 1–5.

(23) Politano, A.; Chiarello, G.; Samnakay, R.; Liu, G.; Gürbulak, B.; Duman, S.; Balandin, A. A.; Boukhvalov, D. W. The Influence of Chemical Reactivity of Surface Defects on Ambient-Stable InSe-Based Nanodevices. *Nanoscale* **2016**, *8*, 8474–8479.

(24) Kistanov, A. A.; Cai, Y.; Zhou, K.; Dmitriev, S. V.; Zhang, Y.-W. Atomic-Scale Mechanisms of Defect- and Light-Induced Oxidation and Degradation of InSe. *J. Mater. Chem. C* **2018**, *6*, 518–525.

(25) Li, X.; Dong, J.; Idrobo, J.-C.; Puretzky, A. A.; Rouleau, C. M.; Geohegan, D. B.; Ding,

F.; Xiao, K. Edge-Controlled Growth and Etching of Two-Dimensional GaSe Monolayers. *J. Am. Chem. Soc.* **2017**, *139*, 482–491.

(26) Gouskov, A.; Camassel, J.; Gouskov, L. Growth and Characterization of III-VI Layered Crystals Like GaSe, GaTe, InSe, GaSe1-XTex and GaxIn1-XSe. *Prog. Cryst. Growth Charact.* **1982**, *5*, 323–413.

(27) Zan, R.; Ramasse, Q. M.; Jalil, R.; Georgiou, T.; Bangert, U.; Novoselov, K. S. Control of Radiation Damage in MoS2 by Graphene Encapsulation. *ACS Nano* **2013**, *7*, 10167–10174.

(28) Algara-Siller, G.; Kurasch, S.; Sedighi, M.; Lehtinen, O.; Kaiser, U. The Pristine Atomic Structure of MoS2 Monolayer Protected from Electron Radiation Damage by Graphene. *Appl. Phys. Lett.* **2013**, *103*, 203107.

(29) Lehnert, T.; Lehtinen, O.; Algara-Siller, G.; Kaiser, U. Electron Radiation Damage Mechanisms in 2D MoSe2. *Appl. Phys. Lett.* **2017**, *110*, 033106.

(30) Nguyen, L.; Komsa, H.-P.; Khestanova, E.; Kashtiban, R. J.; Peters, J. J. P.; Lawlor, S.; Sanchez, A. M.; Sloan, J.; Gorbachev, R. V.; Grigorieva, I. V.; Krasheninnikov, A. V.; Haigh, S. J. Atomic Defects and Doping of Monolayer NbSe2. *ACS Nano* **2017**, *11*, 2894–2904.

(31) Egerton, R. F.; Crozier, P. A.; Rice, P. Electron Energy-Loss Spectroscopy and Chemical Change. *Ultramicroscopy* **1987**, *23*, 305–312.

(32) Egerton, R. F. Mechanisms of Radiation Damage in Beam-Sensitive Specimens, for TEM Accelerating Voltages between 10 and 300 KV. *Microsc. Res. Tech.* **2012**, *75*, 1550–1556.

(33) Egerton, R. F.; Li, P.; Malac, M. Radiation Damage in the TEM and SEM. *Micron* **2004**, *35*, 399–409.

(34) Knotek, M. L.; Feibelman, P. J. Ion Desorption by Core-Hole Auger Decay. *Phys. Rev. Lett.* **1978**, *40*, 964–967.

(35) Guo, Y.; Zhou, S.; Bai, Y.; Zhao, J. Defects and Oxidation of Group-III Monochalcogenide Monolayers. *J. Chem. Phys.* **2017**, *147*, 104709.

(36) Shi, L.; Li, Q.; Ouyang, Y.; Wang, J. Effect of Illumination and Se Vacancies on Fast Oxidation of Ultrathin Gallium Selenide. *Nanoscale* **2018**, *10*, 12180–12186.

(37) Ohta, T.; Klust, A.; Adams, J. A.; Yu, Q.; Olmstead, M. A.; Ohuchi, F. S. Atomic Structures of Defects at GaSe/Si(111) Heterointerfaces Studied by Scanning Tunneling Microscopy. *Phys. Rev. B: Condens. Matter Mater. Phys.* **2004**, *69*, 1–8.

(38) Komsa, H.-P.; Kurasch, S.; Lehtinen, O.; Kaiser, U.; Krasheninnikov, A. V. From Point to Extended Defects in Two-Dimensional MoS2: Evolution of Atomic Structure under Electron Irradiation. *Phys. Rev. B: Condens. Matter Mater. Phys.* **2013**, *88*, 1–8.

(39) Wang, S.; Lee, G. Do; Lee, S.; Yoon, E.; Warner, J. H. Detailed Atomic Reconstruction of Extended Line Defects in Monolayer MoS2. *ACS Nano* **2016**, *10*, 5419–5430.

(40) Liu, H.; Zheng, H.; Yang, F.; Jiao, L.; Chen, J.; Ho, W.; Gao, C.; Jia, J.; Xie, M. Line and Point Defects in MoSe2 Bilayer Studied by Scanning Tunneling Microscopy and Spectroscopy. *ACS Nano* **2015**, *9*, 6619–6625.

(41) Patra, T. K.; Zhang, F.; Schulman, D. S.; Chan, H.; Cherukara, M. J.; Terrones, M.; Das, S.; Narayanan, B.; Sankaranarayanan, S. K. R. S. Defect Dynamics in 2-D MoS2 Probed by Using Machine Learning, Atomistic Simulations, and High-Resolution Microscopy. *ACS Nano* **2018**, *12*, 8006–8016.

(42) Warner, J. H.; Rummeli, M. H.; Bachmatiuk, A.; Buchner, B. Atomic Resolution Imaging and Topography of Boron Nitride Sheet Produced by Chemical Exfoliation. *ACS Nano*

2010, *4*, 1299–1304.

(43) Cretu, O.; Lin, Y. C.; Suenaga, K. Evidence for Active Atomic Defects in Monolayer Hexagonal Boron Nitride: A New Mechanism of Plasticity in Two-Dimensional Materials. *Nano Lett.* **2014**, *14*, 1064–1068.

(44) Pham, T.; Gibb, A. L.; Li, Z.; Gilbert, S. M.; Song, C.; Louie, S. G.; Zettl, A. Formation and Dynamics of Electron-Irradiation-Induced Defects in Hexagonal Boron Nitride at Elevated Temperatures. *Nano Lett.* **2016**, *16*, 7142–7147.

(45) He, K.; Robertson, A. W.; Lee, S.; Yoon, E.; Lee, G. Do; Warner, J. H. Extended Klein Edges in Graphene. *ACS Nano* **2014**, *8*, 12272–12279.

(46) Zhao, X.; Fu, D.; Ding, Z.; Zhang, Y. Y.; Wan, D.; Tan, S. J. R.; Chen, Z.; Leng, K.; Dan, J.; Fu, W.; Geng, D.; Song, P.; Du, Y.; Venkatesan, T.; Pantelides, S. T.; Pennycook, S. J.; Zhou, W.; Loh, K. P. Mo-Terminated Edge Reconstructions in Nanoporous Molybdenum Disulfide Film. *Nano Lett.* **2018**, *18*, 482–490.

(47) Favron, A.; Gaufrès, E.; Fossard, F.; Phaneuf-Laheureux, A. L.; Tang, N. Y. W.; Lévesque, P. L.; Loiseau, A.; Leonelli, R.; Francoeur, S.; Martel, R. Photooxidation and Quantum Confinement Effects in Exfoliated Black Phosphorus. *Nat. Mater.* **2015**, *14*, 826–832.

(48) Clark, N.; Nguyen, L.; Hamer, M. J.; Schedin, F.; Lewis, E. A.; Prestat, E.; Garner, A.; Cao, Y.; Zhu, M.; Kashtiban, R.; Sloan, J.; Kepaptsoglou, D.; Gorbachev, R. V.; Haigh, S. J. Scalable Patterning of Encapsulated Black Phosphorus. *Nano Lett.* **2018**, *18*, 5373–5381.

(49) Wilson, J. A.; Di Salvo, F. J.; Mahajan, S. Charge-Density Waves and Superlattices in the Metallic Layered Transition Metal Dichalcogenides. *Adv. Phys.* **1975**, *24*, 117–201.

(50) Katzke, H.; Toledano, P.; Depmeier, W. Phase Transitions between Polytypes and Intralayer Superstructures in Transition Metal Dichalcogenides. *Phys. Rev. B: Condens. Matter Mater. Phys.* **2004**, *69*, 1–8.

(51) Mishina, E.; Sherstyuk, N.; Lavrov, S.; Sigov, A.; Mitioglu, A.; Anghel, S.; Kulyuk, L. Observation of Two Polytypes of MoS 2 Ultrathin Layers Studied by Second Harmonic Generation Microscopy and Photoluminescence. *Appl. Phys. Lett.* **2015**, *106*, 131901.

(52) Lee, J. U.; Kim, K.; Han, S.; Ryu, G. H.; Lee, Z.; Cheong, H. Raman Signatures of Polytypism in Molybdenum Disulfide. *ACS Nano* **2016**, *10*, 1948–1953.

(53) Terhell, J. C. J. M. Polytypism in the III-VI Layer Compounds. *Prog. Cryst. Growth Charact.* **1983**, *7*, 55–110.

(54) Butz, B.; Dolle, C.; Niekiel, F.; Weber, K.; Waldmann, D.; Weber, H. B.; Meyer, B.; Spiecker, E. Dislocations in Bilayer Graphene. *Nature* **2014**, *505*, 533–537.

(55) Lu, X.; Utama, M. I. B.; Lin, J.; Luo, X.; Zhao, Y.; Zhang, J.; Pantelides, S. T.; Zhou, W.; Quek, S. Y.; Xiong, Q. Rapid and Nondestructive Identification of Polytypism and Stacking Sequences in Few-Layer Molybdenum Diselenide by Raman Spectroscopy. *Adv. Mater.* **2015**, *27*, 4502–4508.

(56) Hovden, R.; Tsen, A. W.; Liu, P.; Savitzky, B. H.; El Baggari, I.; Liu, Y.; Lu, W.; Sun, Y.; Kim, P.; Pasupathy, A. N.; Kourkoutis, L. F. Atomic Lattice Disorder in Charge-Density-Wave Phases of Exfoliated Dichalcogenides (1T-TaS2). *PNAS* **2016**, *113*, 11420–11424.

(57) Rooney, A. P.; Li, Z.; Zhao, W.; Gholinia, A.; Kozikov, A.; Auton, G.; Ding, F.; Gorbachev, R. V.; Young, R. J.; Haigh, S. J. Anomalous Twin Boundaries in Two Dimensional Materials. *Nat. Commun.* **2018**, *9*, 3597.

(58) Wieting, T. J.; Verble, J. L. Interlayer Bonding and the Lattice Vibrations of β-GaSe.

Phys. Rev. B: Condens. Matter Mater. Phys. **1972**, *5*, 1473–1479.

(59) Irwin, J. C.; Hoff, R. M.; Clayman, B. P.; Bromley, R. A. Long Wavelength Lattice Vibrations in GaS and GaSe. *Solid State Commun.* **1973**, *13*, 1531–1536.

(60) Magorrian, S. J.; Zólyomi, V.; Fal'ko, V. I. Spin-Orbit Coupling, Optical Transitions, and Spin Pumping in Monolayer and Few-Layer InSe. *Phys. Rev. B: Condens. Matter Mater. Phys.* **2017**, *96*, 1–6.

(61) Li, Y.; Wang, T.; Wang, H.; Li, Z.; Chen, Y.; West, D.; Sankar, R.; Ulaganathan, R. K.; Chou, F.; Wetzel, C.; Xu, C.-Y.; Zhang, S.; Shi, S. Enhanced Light Emission from the Ridge of Two-Dimensional InSe Flakes. *Nano Lett.* **2018**, *18*, 5078–5084.

(62) Bridgman, P. W. Certain Physical Properties of Single Crystals of Tungsten, Antimony, Bismuth, Tellurium, Cadmium, Zinc, and Tin. *Proc. Am. Acad. Arts Sci.* **1925**, *60*, 305.

(63) Kokh, K. A.; Andreev, Y. M.; Svetlichnyi, V. A.; Lanskii, G. V.; Kokh, A. E. Growth of GaSe and GaS Single Crystals. *Cryst. Res. Technol.* **2011**, *46*, 327–330.

(64) Cao, Y.; Mishchenko, A.; Yu, G. L.; Khestanova, E.; Rooney, A. P.; Prestat, E.; Kretinin, A. V.; Blake, P.; Shalom, M. Ben; Woods, C. R.; Chapman, J.; Balakrishnan, G.; Grigorieva, I. V.; Novoselov, K. S.; Piot, B. A.; Potemski, M.; Watanabe, K.; Taniguchi, T.; Haigh, S. J.; *et al*. Quality Heterostructures from Two-Dimensional Crystals Unstable in Air by Their Assembly in Inert Atmosphere. *Nano Lett.* **2015**, *15*, 4914–4921.

(65) Frisenda, R.; Navarro-Moratalla, E.; Gant, P.; Pérez De Lara, D.; Jarillo-Herrero, P.; Gorbachev, R. V.; Castellanos-Gomez, A. Recent Progress in the Assembly of Nanodevices and van Der Waals Heterostructures by Deterministic Placement of 2D Materials. *Chem. Soc. Rev.* **2018**, *47*, 53–68.

(66) Koch, C. Determination of Core Structure Periodicity and Point Defect Density Along

Dislocations, Ph.D., Arizona State University, 2002.

(67) Bergerhoff, G.; Brown, I. D. Crystallographic Databases. In *International Union of Crystallography*; Chester, 1987; pp 77–95.

(68) Hjorth Larsen, A.; Jørgen Mortensen, J.; Blomqvist, J.; Castelli, I. E.; Christensen, R.; Dułak, M.; Friis, J.; Groves, M. N.; Hammer, B.; Hargus, C.; Hermes, E. D.; Jennings, P. C.; Bjerre Jensen, P.; Kermode, J.; Kitchin, J. R.; Leonhard Kolsbjerg, E.; Kubal, J.; Kaasbjerg, K.; Lysgaard, S.; *et al*. The Atomic Simulation Environment — a Python Library for Working with Atoms. *J. Phys. Condens. Matter* **2017**, *29*, 273002.

(69) Momma, K.; Izumi, F. VESTA 3 for Three-Dimensional Visualization of Crystal, Volumetric and Morphology Data. *J. Appl. Crystallogr.* **2011**, *44*, 1272–1276.

(70) de la Peña, F.; Ostasevicius, T.; Tonaas Fauske, V.; Burdet, P.; Jokubauskas, P.; Nord, M.; Sarahan, M.; Prestat, E.; Johnstone, D. N.; Taillon, J.; Caron, J.; Furnival, T.; MacArthur, K. E.; Eljarrat, A.; Mazzucco, S.; Migunov, V.; Aarholt, T.; Walls, M.; Winkler, F.; *et al*. Electron Microscopy (Big and Small) Data Analysis With the Open Source Software Package HyperSpy. *Microsc. Microanal.* **2017**, *23*, 214–215.

(71) Verbeeck, J.; Van Aert, S. Model Based Quantification of EELS Spectra. *Ultramicroscopy* **2004**, *101*, 207–224.

(72) Kresse, G.; Furthmüller, J. Efficient Iterative Schemes for *Ab Initio* Total-Energy Calculations Using a Plane-Wave Basis Set. *Phys. Rev. B: Condens. Matter Mater. Phys.* **1996**, *54*, 11169–11186.

(73) Ben Aziza, Z.; Zólyomi, V.; Henck, H.; Pierucci, D.; Silly, M. G.; Avila, J.; Magorrian, S. J.; Chaste, J.; Chen, C.; Yoon, M.; Xiao, K.; Sirotti, F.; Asensio, M. C.; Lhuillier, E.; Eddrief, M.; Fal'Ko, V. I.; Ouerghi, A. Valence Band Inversion and Spin-Orbit Effects in

the Electronic Structure of Monolayer GaSe. *Phys. Rev. B* **2018**, *98*, 1–7.

For Table of Contents Only